Supporting Information

Defect Formation and Healing at Grain Boundaries in Lead-Halide Perovskites

Waldemar Kaiser,[1*] Kashif Hussain,[2,3] Ajay Singh,[4] Asma A. Alothman,[5] Daniele Meggiolaro,[1] Alessio Gagliardi,[2] Edoardo Mosconi,[1,5*] Filippo De Angelis[1,6]

[1]*Computational Laboratory for Hybrid/Organic Photovoltaics (CLHYO), Istituto CNR di Scienze e Tecnologie Chimiche "Giulio Natta" (CNR-SCITEC), Via Elce di Sotto 8, 06123 Perugia, Italy.*

[2]*Department of Electrical and Computer Engineering, Technical University of Munich, Hans-Piloty-Straße 1, 85748 Garching, Germany.*

[3]*Department of Electrical Engineering, Sukkur IBA University, 65200 Sukkur, Pakistan.*

[4]*Department of Physics and Materials Science, University of Luxembourg, Luxembourg L-1511, Luxembourg.*

[5]*Chemistry Department, College of Science, King Saud University, Riyadh 1451, Kingdom of Saudi Arabia.*

[6]*Department of Chemistry, Biology and Biotechnology, University of Perugia and UdR INSTM, Via Elce di Sotto 8, 06123 Perugia, Italy.*

Corresponding Author

E-Mail: waldemar.kaiser@scitec.cnr.it ; edoardo@thch.unipg.it

S1. Identification and Classification of Split Interstitials

We analyze each snapshot of the AIMD trajectory on the $CsPbI_3$ grain boundary model as follows. First, all lead-iodine bonds are determined using a cutoff distance of 3.7 Å. The choice of the cutoff distance is to account for the strong dynamical fluctuations in the lead-iodine bonds. For all pairs of Pb atoms (Pb_A, Pb_B), we determine the amount of I atoms which form bonds with both Pb_A and Pb_B. In the typical crystal structure of $CsPbI_3$ we expect maximum **1** I atom bonded to a pair of Pb atoms. If, however, the pair (Pb_A, Pb_B) shares **2** I atoms, a split interstitial is present.

S2. Additional Figures

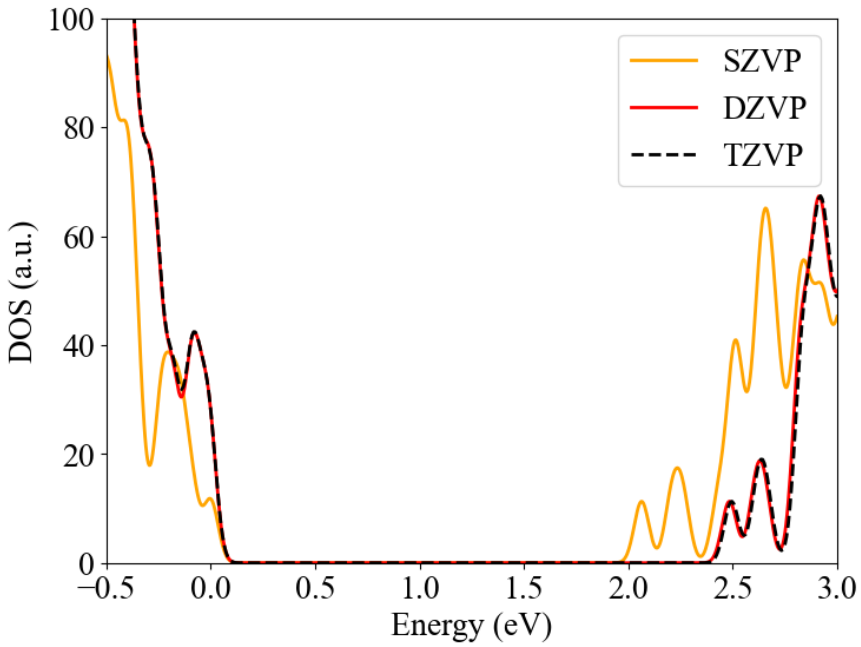

Figure S1. Convergence test of the basis set on the density of states within CP2K. For computational details, we refer to section 2 of the manuscript.

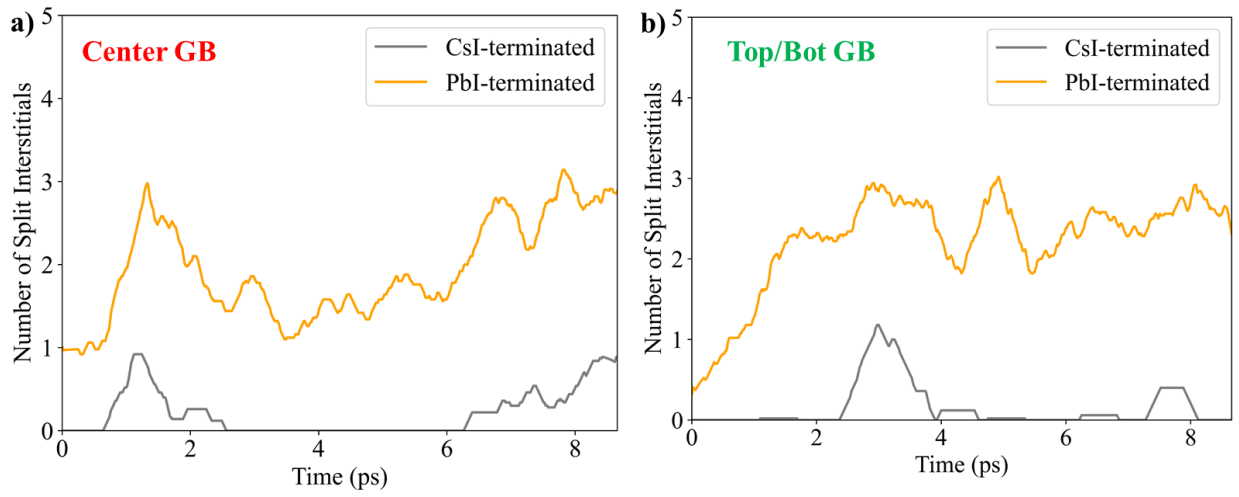

Figure S2. Time evolution of the number of split interstitials in the (yellow) PbI-terminated and in the (grey) CsI-terminated region in (a) the center GB and (b) the top/bot GB.

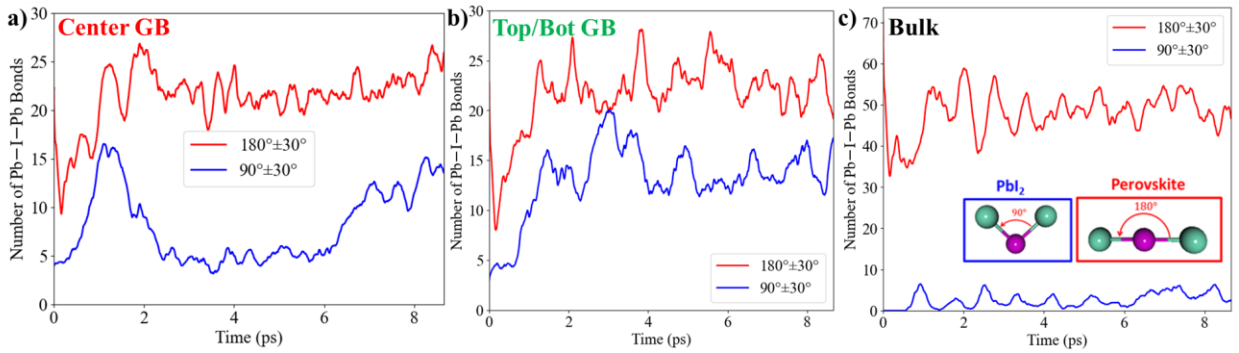

Figure S3. Time evolution of the number of 90° and 180° Pb–I–Pb bond angles in the (a) top/bot GB, (b) the center GB, and (b) in the bulk region.

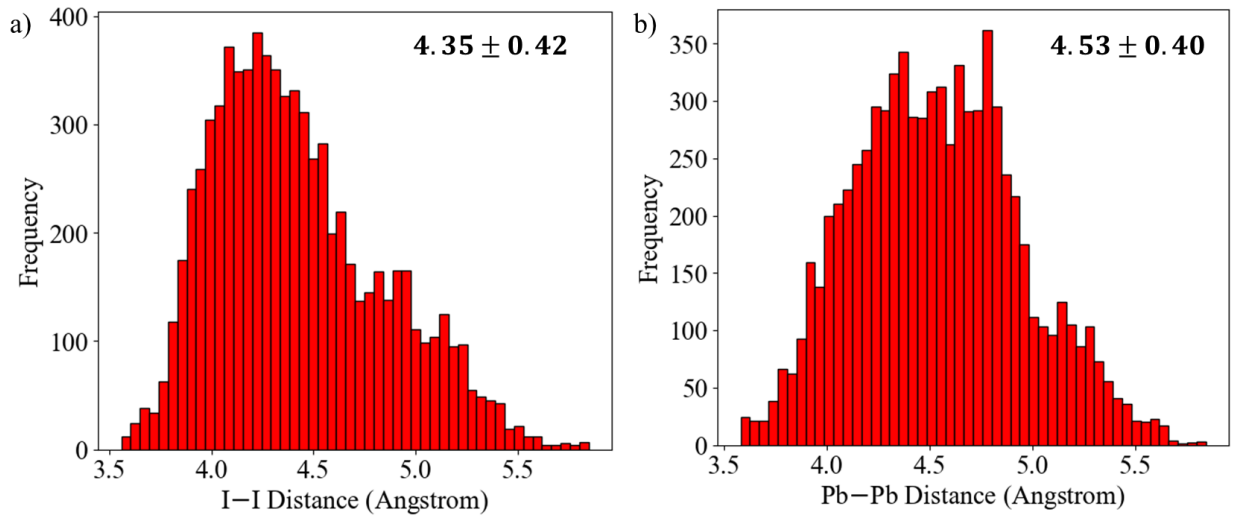

Figure S4. (a) Distribution of the I–I distance of all split interstitials within the CPMD trajectory. (b) Distribution of the Pb–Pb distance of all split interstitials from *ab initio* molecular dynamics simulations.

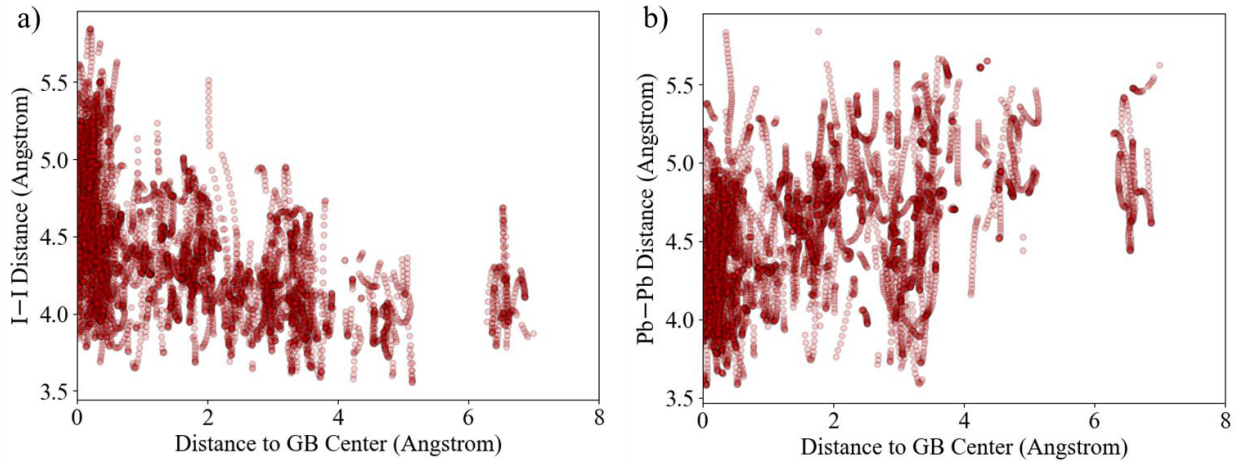

Figure S5. (a) I–I distance and (b) Pb–Pb distance versus distance to the center of the nearest GB for all split interstitials from *ab initio* molecular dynamics simulations.

Table S1. Evaluation of the average geometry of the Frenkel-type defects. Reported are averages and standard deviations for the Pb–Pb distance, average I–I distance between all split iodine interstitial ions, and the average Pb–I bond length, as well as the average number of appearances of the respective configuration throughout the *ab initio* molecular dynamics simulations.

Frenkel Defect	**Pb–Pb distance (Å)**	**I–I distance (Å)**	**Pb–I bond length (Å)**	**Avg. appearance**
I_i^-	4.51 ± 0.32	4.29 ± 0.50	3.55 ± 0.09	0.07
I_i^-/V_I^+	4.53 ± 0.41	4.38 ± 0.41	3.55 ± 0.11	1.58
$I_i^-/2V_I^+$	4.53 ± 0.41	4.36 ± 0.40	3.53 ± 0.12	0.99
$2I_i^-/2V_I^+$	4.48 ± 0.40	4.32 ± 0.49	3.53 ± 0.09	0.24

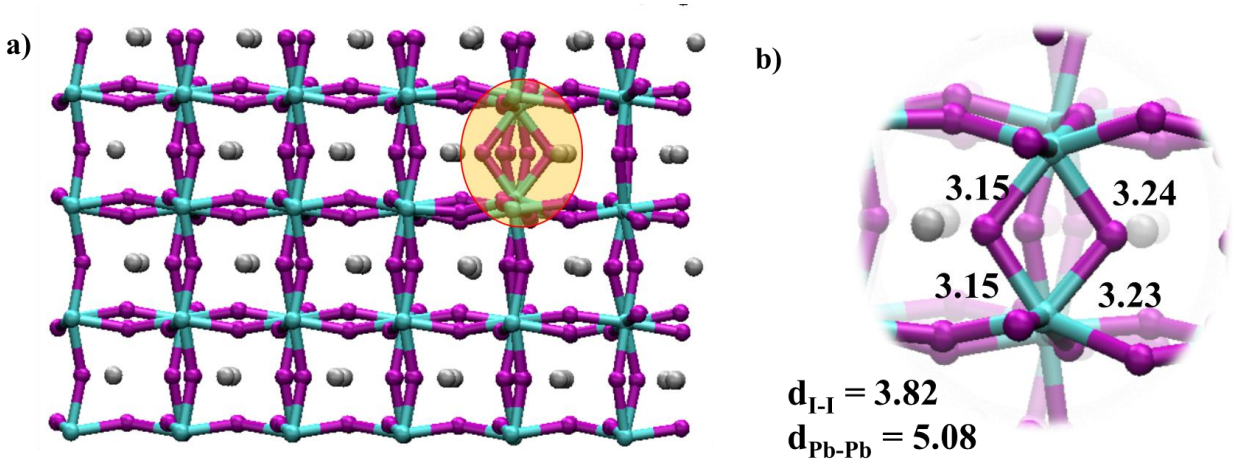

Figure S6. (a) $CsPbI_3$ crystal structure with an I_i^- interstitial (highlighted). (b) Pb–I bond lengths and I–I as well as Pb–Pb distances of the I_i^- interstitial in the optimized $CsPbI_3$ crystal.

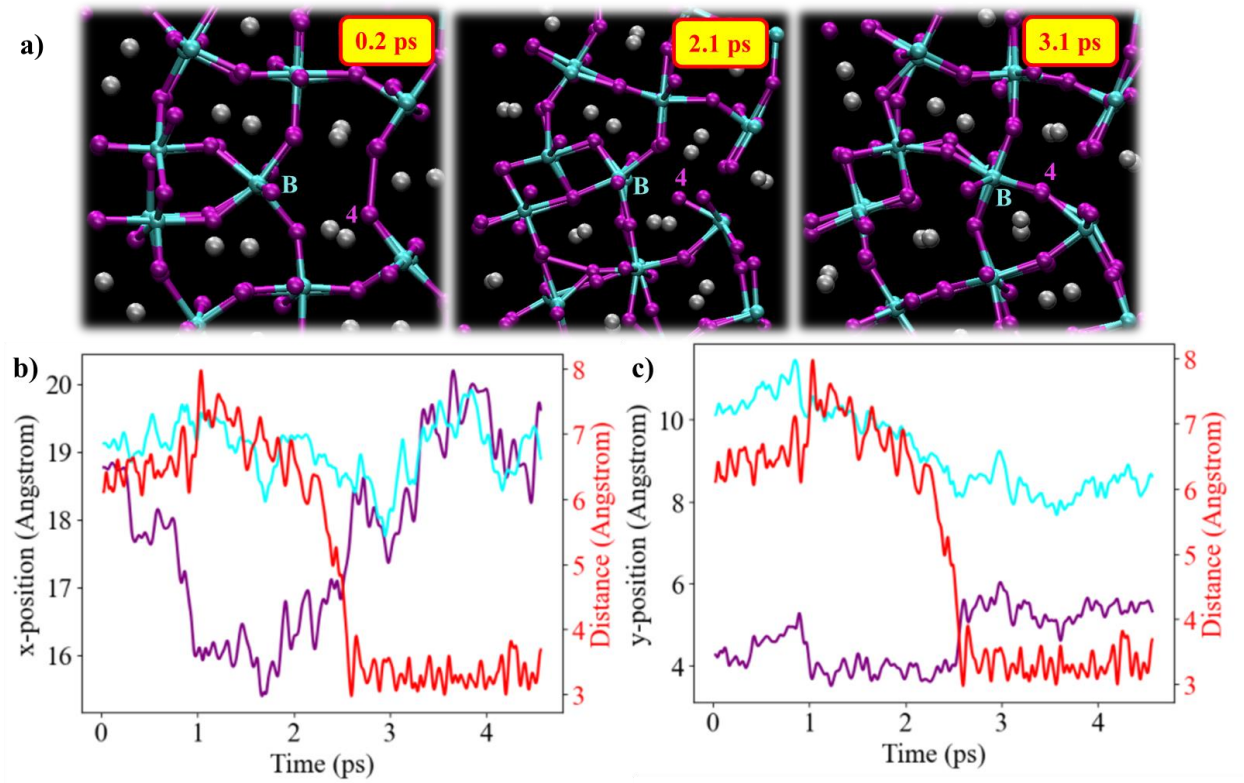

Figure S7. (a) Snapshots visualizing the mechanism of the Pb(B)–I(4) bond formation. (b) and (c) illustrate the Pb(B)–I(4) distance and the position of I(4) in purple and of Pb(B) in cyan in x and y direction, respectively.

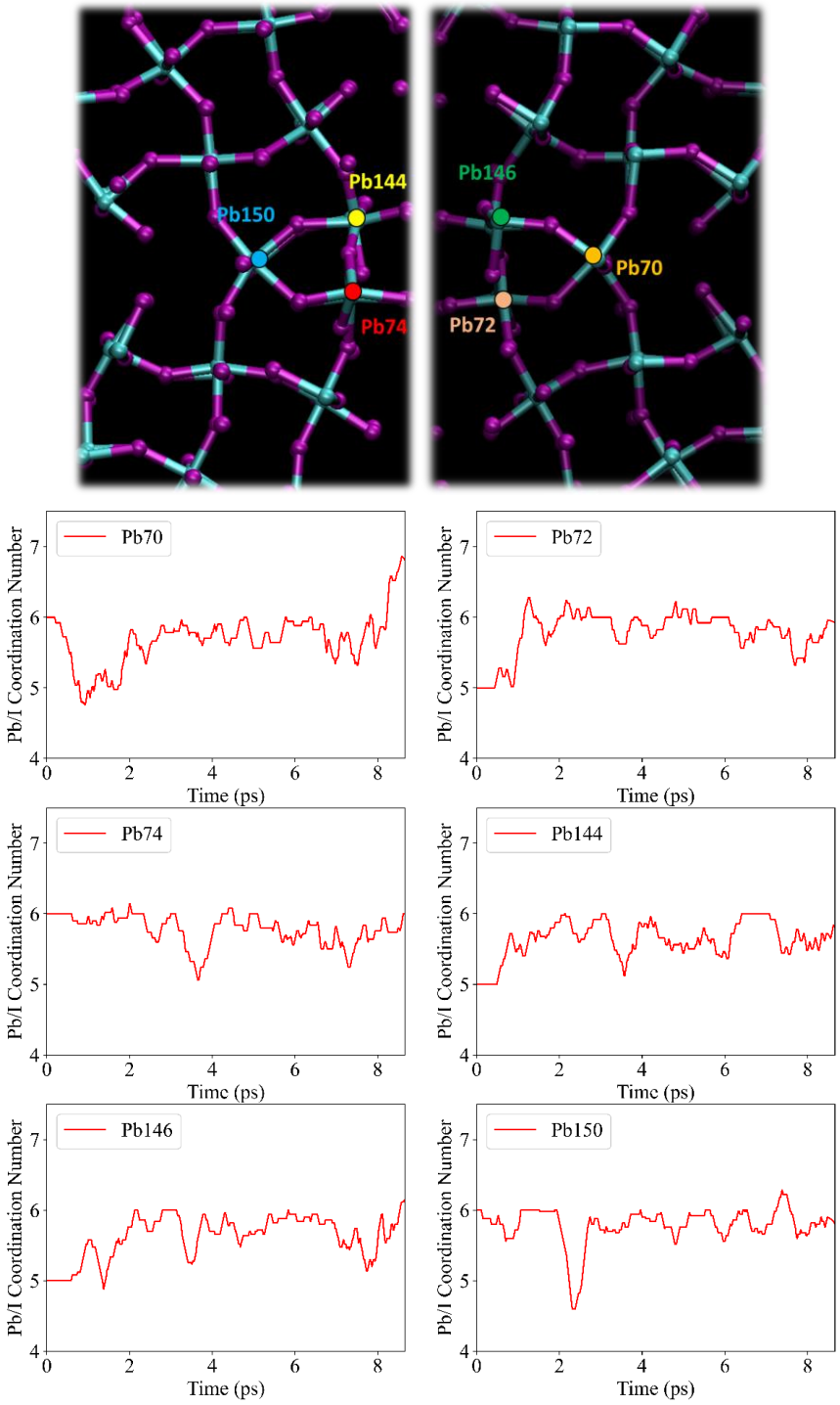

Figure S8. (Top) Label of Pb ions in the center GB, showing the (left) front view and (right) back view. (Bottom) Time evolution of the Pb/I coordination number for each Pb ion in the center grain boundary.

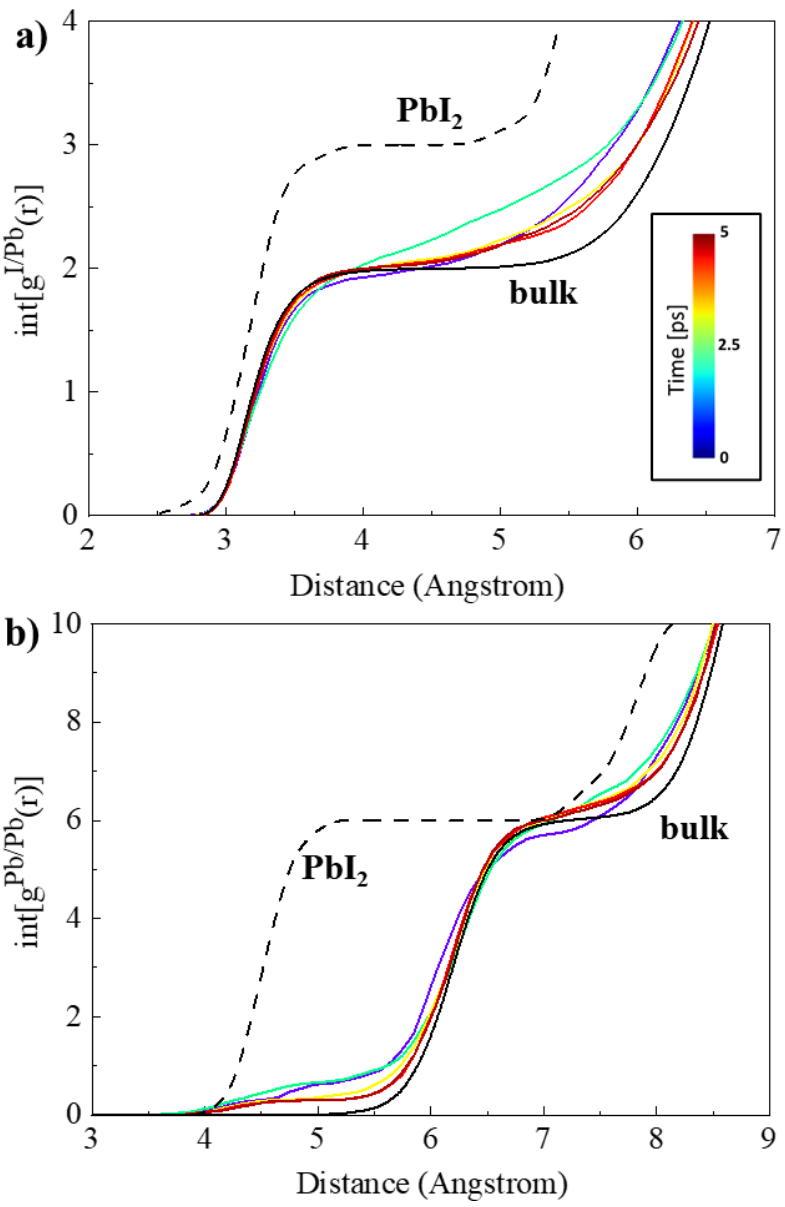

Figure S9. Temporal evolution of the integral of the radial pair distribution function for (a) I/Pb and (b) Pb/Pb between t = 0 ps and t = 5 ps. The solid black curve illustrates the bulk values in $CsPbI_3$ (see also Figure S8 and S9, Supporting Information), and the dashed line in (a) and (b) gives the int[g(r)] for PbI_2.

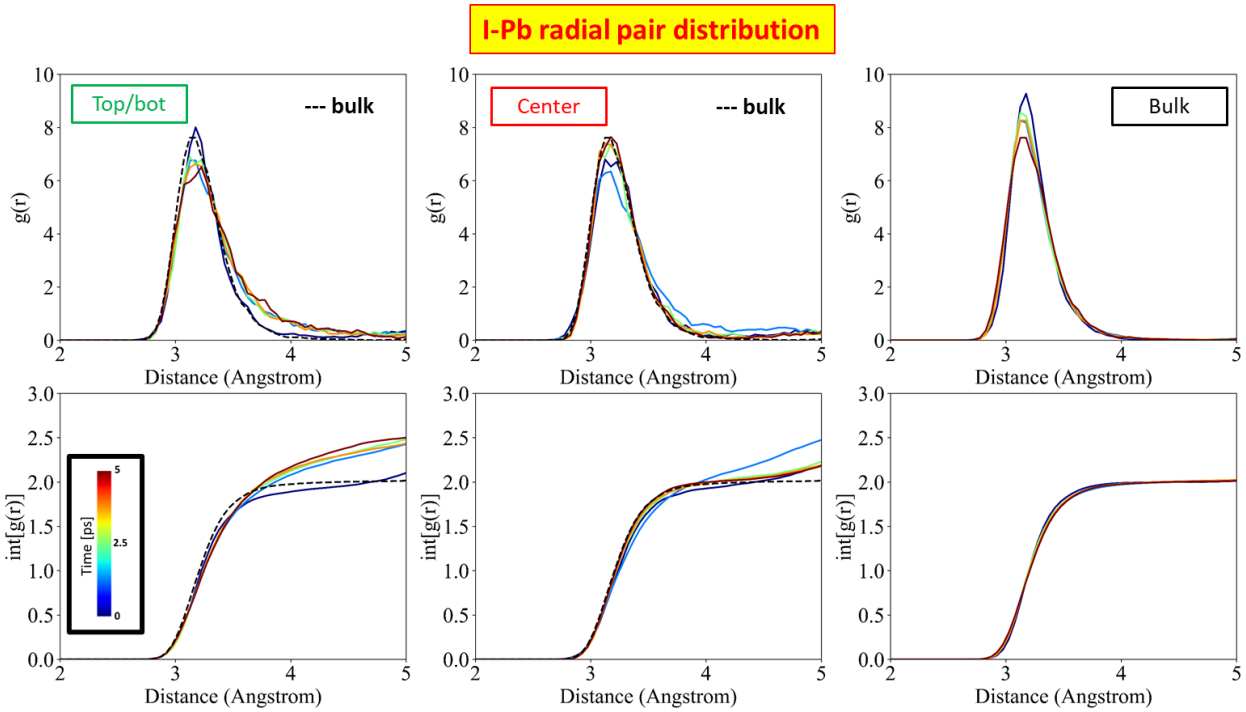

Figure S10. Time evolution of the I/Pb radial pair distribution function, g(r), and its integral int[g(r)] for the (left) top/bot GB, (middle) the center GB, and (right) the bulk. The dashed lines give the g(r) and int[g(r)] of the bulk $CsPbI_3$. The color legend is given in the lower left panel

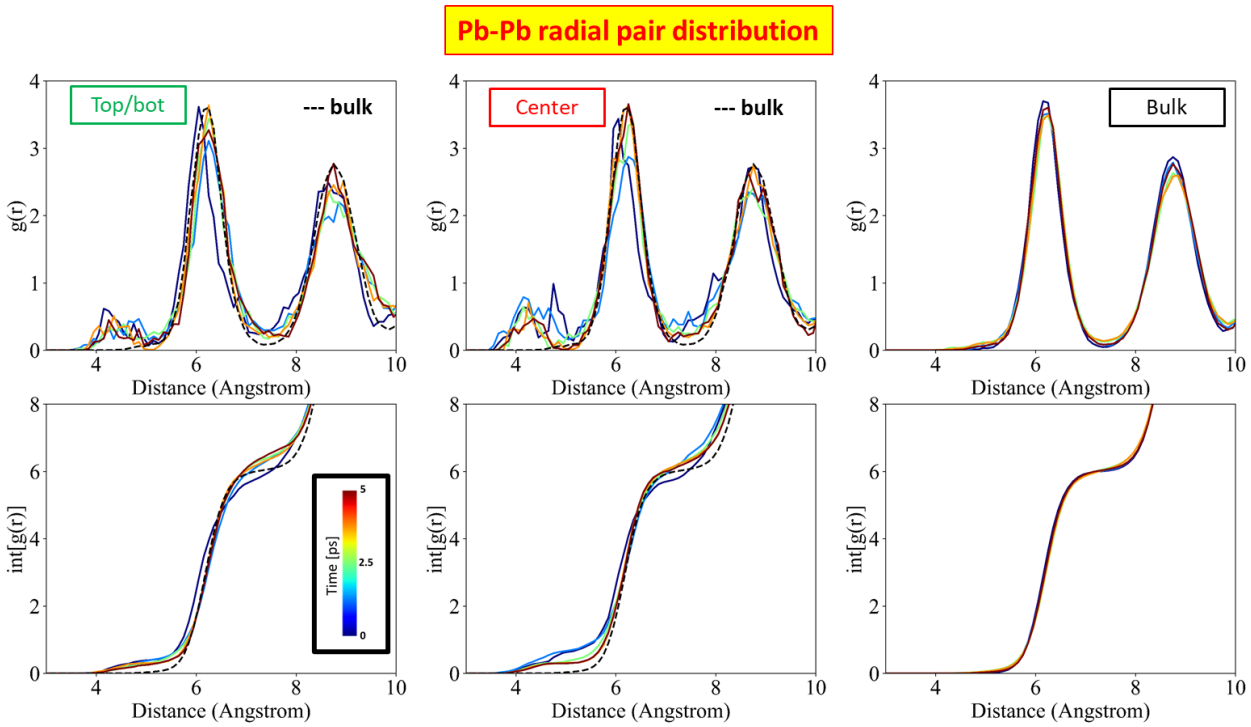

Figure S11. Time evolution of the Pb/Pb radial pair distribution function, g(r), and its integral int[g(r)] for the (left) top/bot GB, (middle) the center GB, and (right) the bulk. The dashed lines give the g(r) and int[g(r)] of the bulk $CsPbI_3$. The color legend is given in the lower left panel

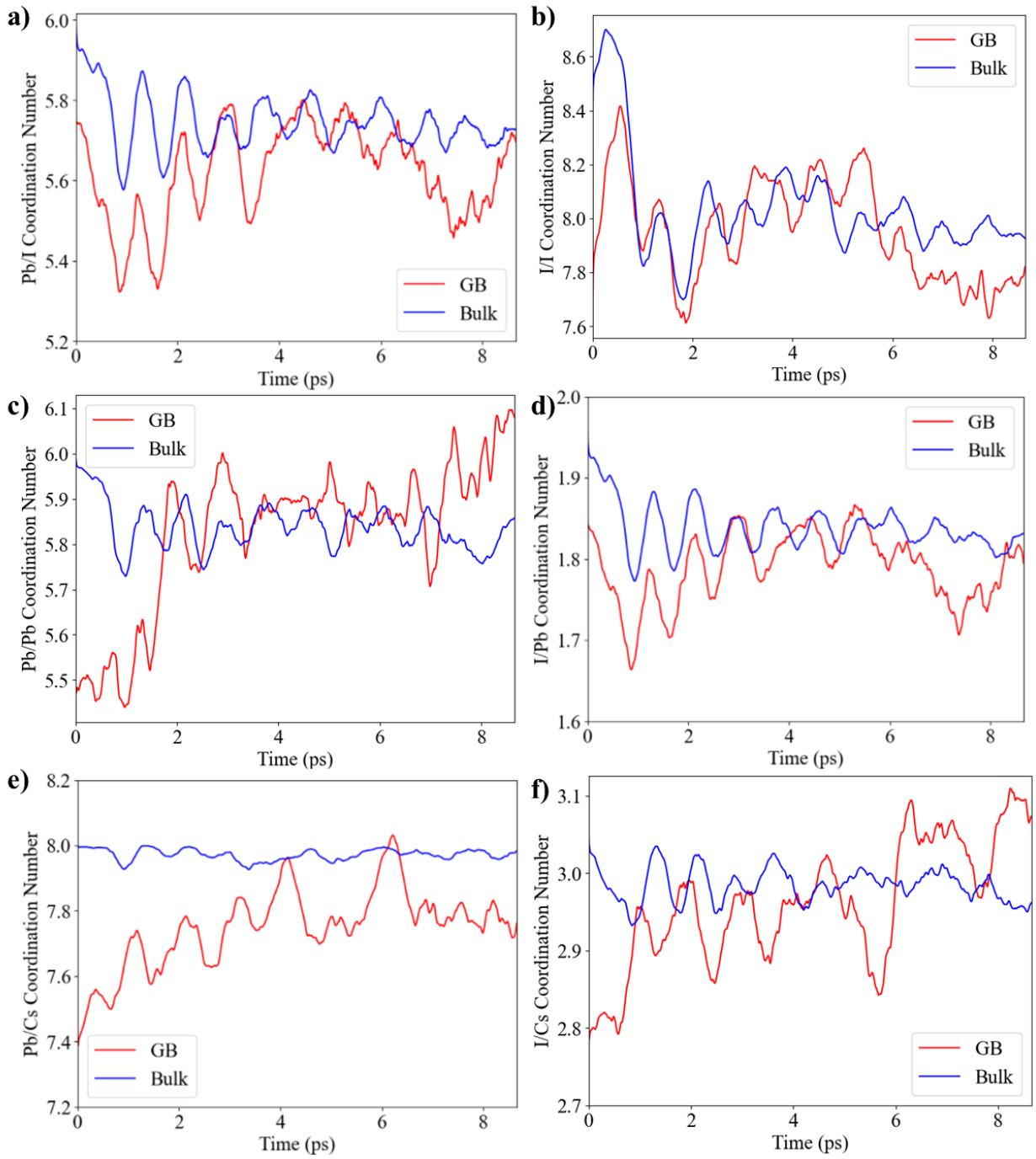

Figure S12. Time evolution of the (a) Pb/I, (b) I/I, (c) Pb/Pb, (d) I/Pb, (e) Pb/Cs, and (f) I/Cs coordination number in the bulk (blue curves) and in the center grain boundary (red curves).

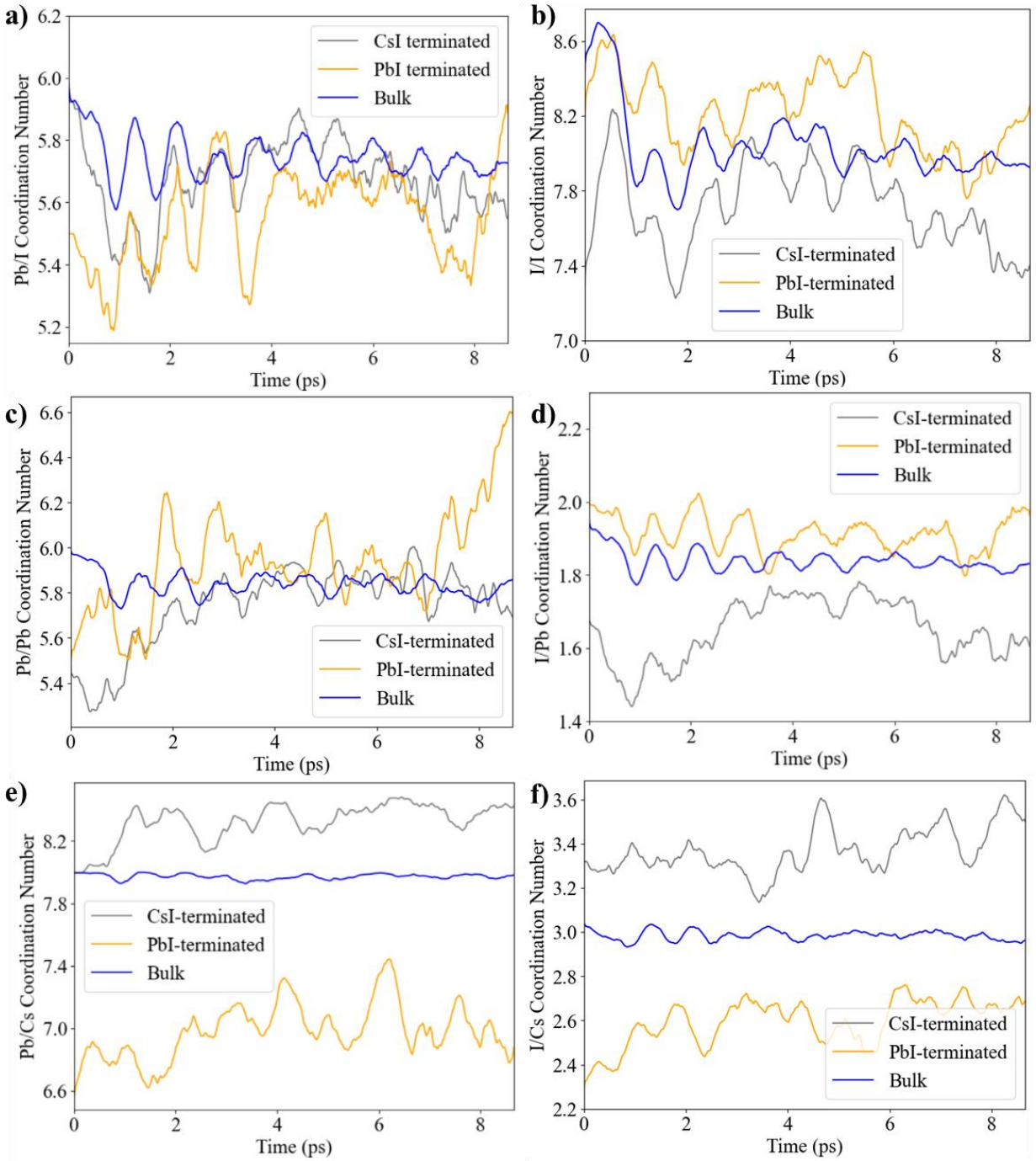

Figure S13. Time evolution of the (a) Pb/I, (b) I/I, (c) Pb/Pb, (d) I/Pb, (e) Pb/Cs, and (f) I/Cs coordination number in the bulk (blue curves) and in the PbI- (yellow curves) and in the CsI-terminated (grey curves) region in the center grain boundary.

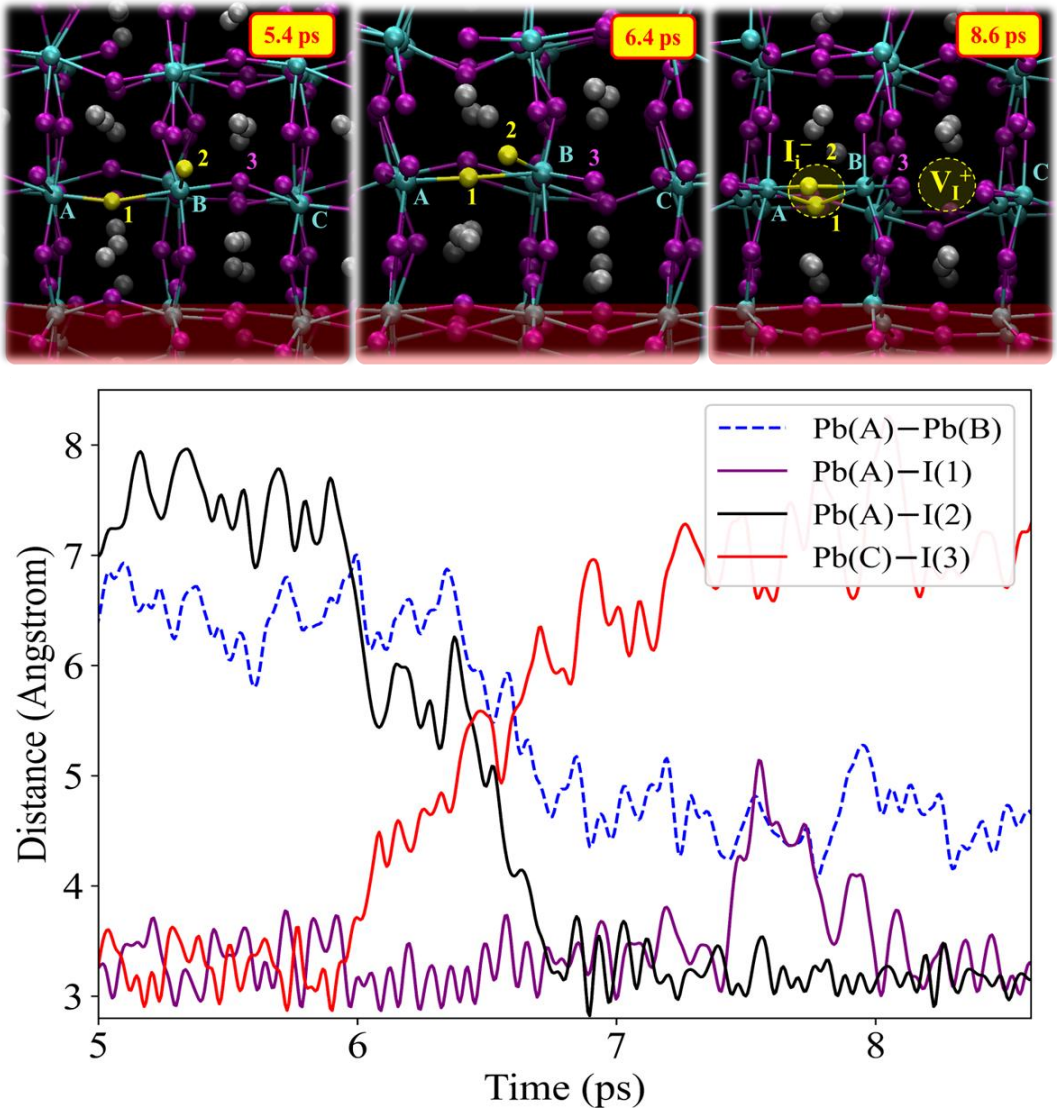

Figure S14. (Top) Snapshots visualizing the key steps during the bulk iodine Frenkel defect formation. Letters and numbers consistently label the Pb and the I ions, respectively. (Bottom) Time evolution of lead – iodine distances during Frenkel formation.

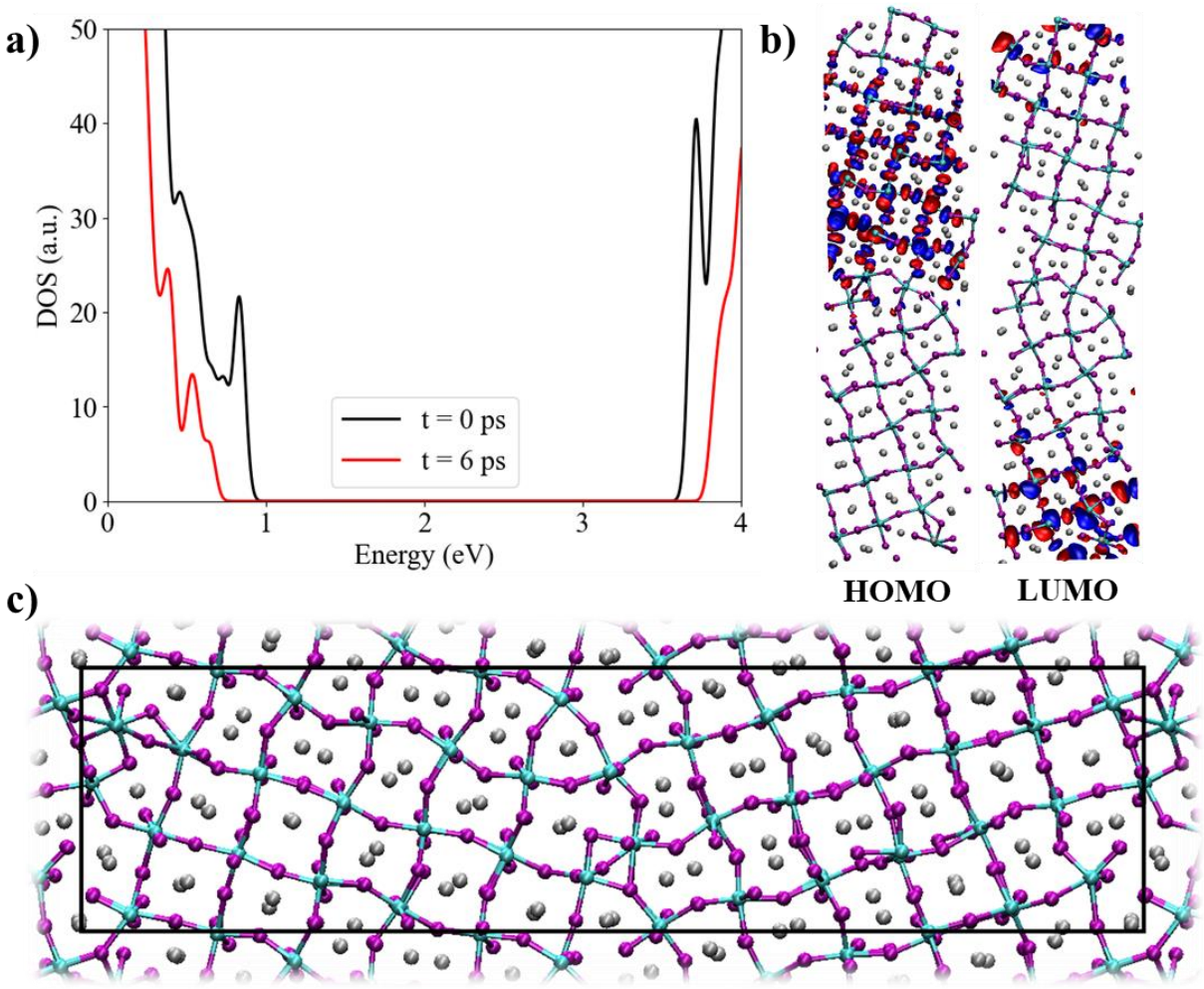

Figure S15. (a) Density of states of the optimized structures at t = 0 ps and at t = 6 ps. The energy of the 6 ps structure is of 1.03 eV lower than one of the initial structure. (b) HOMO and LUMO orbitals of the optimized structure at 4 ps. (c) Visualization of the optimized structure at t = 6 ps.

Table S2. Scf energies of the optimized grain boundary structures. We relaxed the ionic positions starting from the AIMD positions at t = {0, 2, 4, 6, 8} ps to a force threshold of 0.001 Ry/B^3. ΔE gives the energy difference with respect to the initial configuration at 0 ps.

Configuration	Scf Energy (Ry)	ΔE (eV)
0 ps	-28114.05472497	0
2 ps	-28114.08002343	-0.344
4 ps	-28114.12294985	-0.928
6 ps	-28114.13015124	-1.026
8 ps	-28114.09950294	-0.609

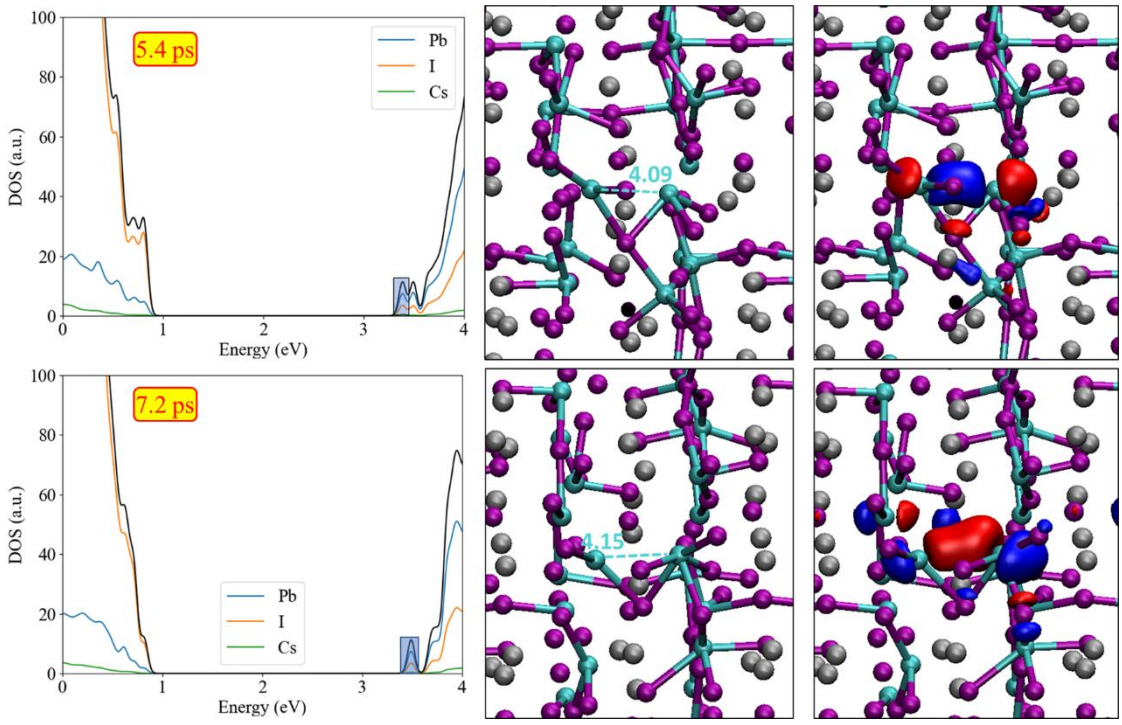

Figure S16. Analysis of shallow trap states near the conduction band minimum at 5.4 ps and at 7.2 ps, including the (left) DOS, (mid) geometry, and (right) orbital of the trap state. The trap states are attributed to Pb–Pb bonding states, localized between Pb ions separated by 4.09 and 4.15 Å.

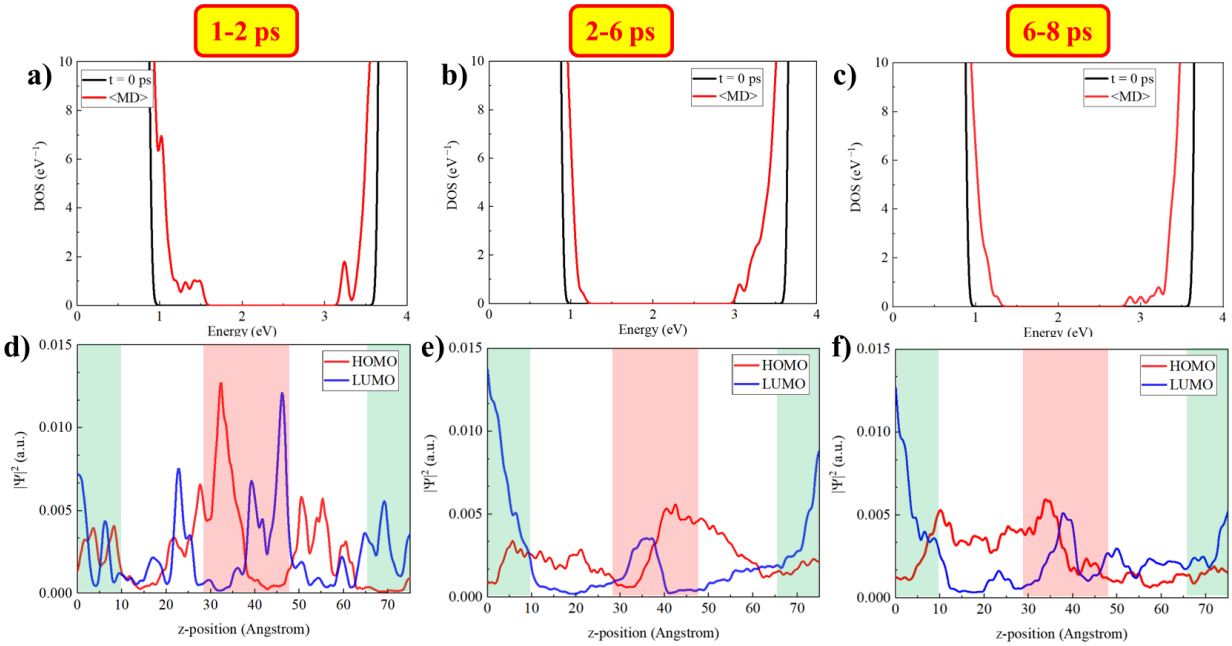

Figure S17. (a) to (c): Density of states of the initial configuration (t = 0 ps) and averaged density of states, <MD>, on the AIMD snapshots for each 0.1 ps. (d) to (f): Averaged probability distribution $|\psi|_2$ for the HOMO and the LUMO across the z-position. The GB regions are highlighted in red and green for the center and the top/bottom GB, respectively.

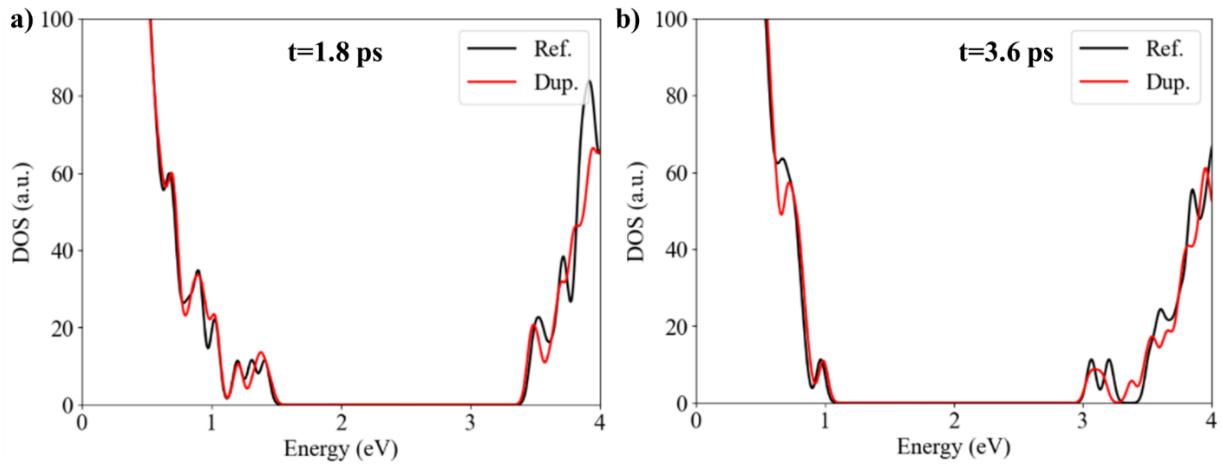

Figure S18. Density of states of two snapshots for supercell of a=12.695 Å, b=19.242 Å, c=76.972 Å (reference) and for the duplicated cells along the short axis (a=25.39 Å, b=19.242 Å, c=76.972 Å). Band edges and mid gap states are well captured by the reference system, which allows us to do single point calculations on the electronic structure based on the reference structure.

S3. Drift-Diffusion Simulation Model

To investigate the impact of grain boundaries on the photovoltaic performance, we use a finite element drift-diffusion model in 1-dimensional (1D) space. The model is implemented in TiberCAD multiscale simulation tool,[1,2] and is based on numerically solving the drift-diffusion (DD) equations. The implemented model has already been used for the simulating perovskite solar cells,[3,4] dye sensitized solar cells,[5-7] organic solar cells,[8,9] and light emitting diodes.[10,11] The model considers the generation of electron-hole pairs upon light absorption and charge carrier transport simultaneously.

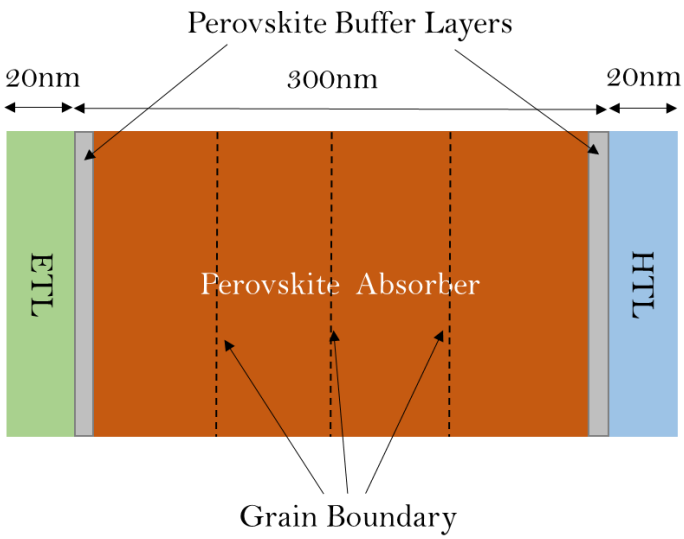

Figure S19. Schematic diagram of the one-dimensional perovskite solar cell model.

The device model for the perovskite solar cell, Figure S16, consists of an electron transport layer (ETL), perovskite absorber, hole transport layer (HTL), and two thin buffer layers on each side of the perovskite to account for interface traps. Grain boundaries are modeled as 2 nm thick regions consisting of trap states and/or a shift in the conduction band minima.

The charge carrier transport is governed by diffusion and electrically induced drift. We ignore the role of ionic defects for simplicity. The Poisson equation used in the simulation is:

$$\nabla \cdot (\epsilon \nabla \phi) = -q(n - p + N_a^- - N_d^+ + n_t^- - n_t^+) \qquad (1)$$

The continuity equations for the charge carriers are given as:

$$\nabla \cdot \{\mu_n n(\nabla \Phi_n)\} = G - R \qquad \text{for electrons} \qquad (2)$$

$$\nabla \cdot \{\mu_p p(\nabla \Phi_p)\} = -(G - R) \qquad \text{for holes} \qquad (3)$$

Here, the electrostatic potential ϕ is a variable dependent on the charge carrier distribution. ϵ is the material dielectric permittivity, q is the electron charge, and n, p are the electron and hole densities, respectively. N_a^-, N_d^+ are the ionized acceptor and donor impurities, respectively. n_t^-, n_t^+

represent the donor and acceptor trap densities, respectively. μ_n, μ_p denote the electron and hole mobility, respectively, and Φ_n, Φ_p are the electron and hole electrochemical potentials, respectively. Net charge carrier generation and recombination rates are represented by *G* and *R*, respectively.

Photogeneration in the perovskite absorber and the buffer regions is governed by the Lambert-Beer absorption model, with the electron-hole (e-h) pair generation at position *z* governed by:

$$G(z) = \int_{\lambda_{\min}}^{\lambda_{\max}} \varphi\,(\lambda)\alpha\,(\lambda)\exp(-\alpha(\lambda)z)\,\mathrm{d}\lambda \tag{4}$$

where $\varphi(\lambda)$ is the intensity of solar irradiation, and α is the absorption coefficient. For simplicity, the maximum e-h pair generation rate used in the simulation is $1.2 \times 10^{22}\ \mathrm{cm^{-3}s^{-1}}$, which corresponds to absorption coefficient of approximately $8\ \mu\mathrm{m}^{-1}$. The direct (radiative) recombination of the charge carriers is calculated as:

$$R_d = k_d\,(np - n_i^2) \tag{5}$$

where, k_d is the direct recombination constant and n_i is the intrinsic charge carrier concentration. To account for the trap effect, the second recombination mechanism is represented by Shockley-Read-Hall (SRH) recombination rate:

$$R_{\mathrm{SRH}} = N_t\,\frac{v_{th}^n\,\sigma^n v_{th}^p\,\sigma^p(np-n_i^2)}{v_{th}^n\,\sigma^n\,(n+n_c)+\,v_{th}^p\,\sigma^p\,(p+p_v)} \tag{6}$$

where, N_t is the trap density, σ^n, σ^p are the capture cross sections, v_{th}^n, v_{th}^p are thermal velocities of electrons and holes, respectively. n_c, p_v are defined as:

$$n_c = N_c \exp\left(\frac{E_T - E_c}{k_B T}\right), \tag{7}$$

$$p_v = N_v \exp\left(\frac{E_v - E_T}{k_B T}\right) \tag{8}$$

where, N_c, and N_v are the effective density of states (DOS) of conduction and valence bands, respectively. E_T, E_c and E_v are the energy levels for the traps, conduction band and valence band, respectively. k_B is the Boltzmann constant, and T is the absolute temperature. For our simulation model, trap states are introduced below the conduction maximum to study their impact on the device performance. All the simulations are done at T=300 K. To obtain a reasonable parametrization, we chose material parameters of the well-studied methylammonium lead iodide perovskite absorber, as the A-site cation has a negligible impact on the frontier orbitals and defect energy levels. The parameters used for the drift-diffusion simulation are summarized in Table S1.

Table S3. Simulation parameters used for drift-diffusion simulations.

Parameter	Value	Reference
Perovskite thickness	300 nm	--
Perovskite bandgap	1.55 eV	[12]
Perovskite valence band edge	-5.43 eV	[12]
Electron and hole mobility	5 $cm^2V^{-1}s^{-1}$	[13]
Perovskite relative permittivity	24.1	[14]
Electron mobility in TiO_2	0.02 $cm^2V^{-1}s^{-1}$	[15]
TiO_2 HOMO	-7.2 eV	[15]
TiO_2 bandgap	3.2 eV	[15]
TiO_2 relative permittivity	85	[19]
Hole mobility SpiroOMeTAD	0.01 $cm^2V^{-1}s^{-1}$	[16]
SpiroOMeTAD HOMO	-5.22 eV	[17]
SpiroOMeTAD bandgap	3.17 eV	[17]
SpiroOMeTAD relative permittivity	3	[18]
Doping SpiroOMeTAD	4.8×10^{17} cm^{-3}	[22]
Cathode fermi level	-5.2 eV	[21]
Anode fermi level	-4.05 eV	fit
Grain Boundary trap density	$10^{14} - 10^{17}$ cm^{-3}	--
Interface trap density	2×10^{15} cm^{-3}	fit

Capture cross section electrons (σ_n)	2×10^{-14} cm^2	[23]
Capture cross section holes (σ_p)	2×10^{-14} cm^2	[23]
Direct recombination rate	5×10^{-11} cm^{-3} s^{-1}	(20)
Maximum generation rate	1.2×10^{22} cm^{-3}	--

The J-V characteristics of the cell are calculated at different conduction band energy and trap energy levels in the grain boundary regions. To account for the effects of interface traps, the interface trap density is fixed at 2×10^{15} cm^{-3}, while the trap density at the grain boundary regions is varied between 1×10^{14} and 1×10^{17} cm^{-3}. The combined results show a deteriorated device performance for increasing trap density and trap energy as shown in Figures S18 to S21.

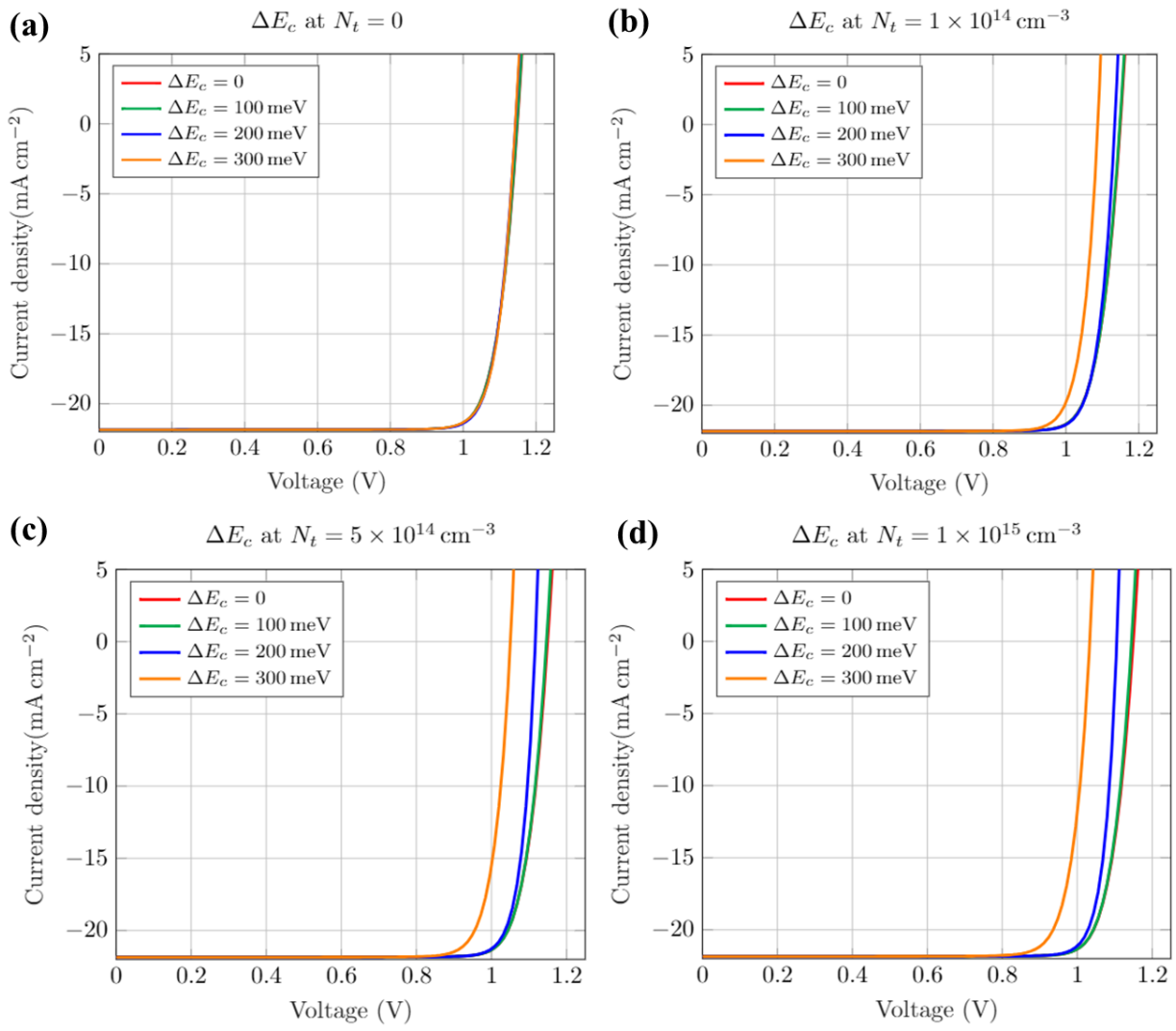

Figure S20. Calculated J-V characteristics for different conduction band energy shift within grain boundary regions. The trap density at the GB region is considered to be (a) 0 cm^{-3}, (b) 1×10^{14} cm^{-3}, (c) 5×10^{14} cm^{-3} , and (d) 1×10^{15} cm^{-3}. The trap energy is considered to be the same as conduction band minimum, i.e. $E_t = 0$.

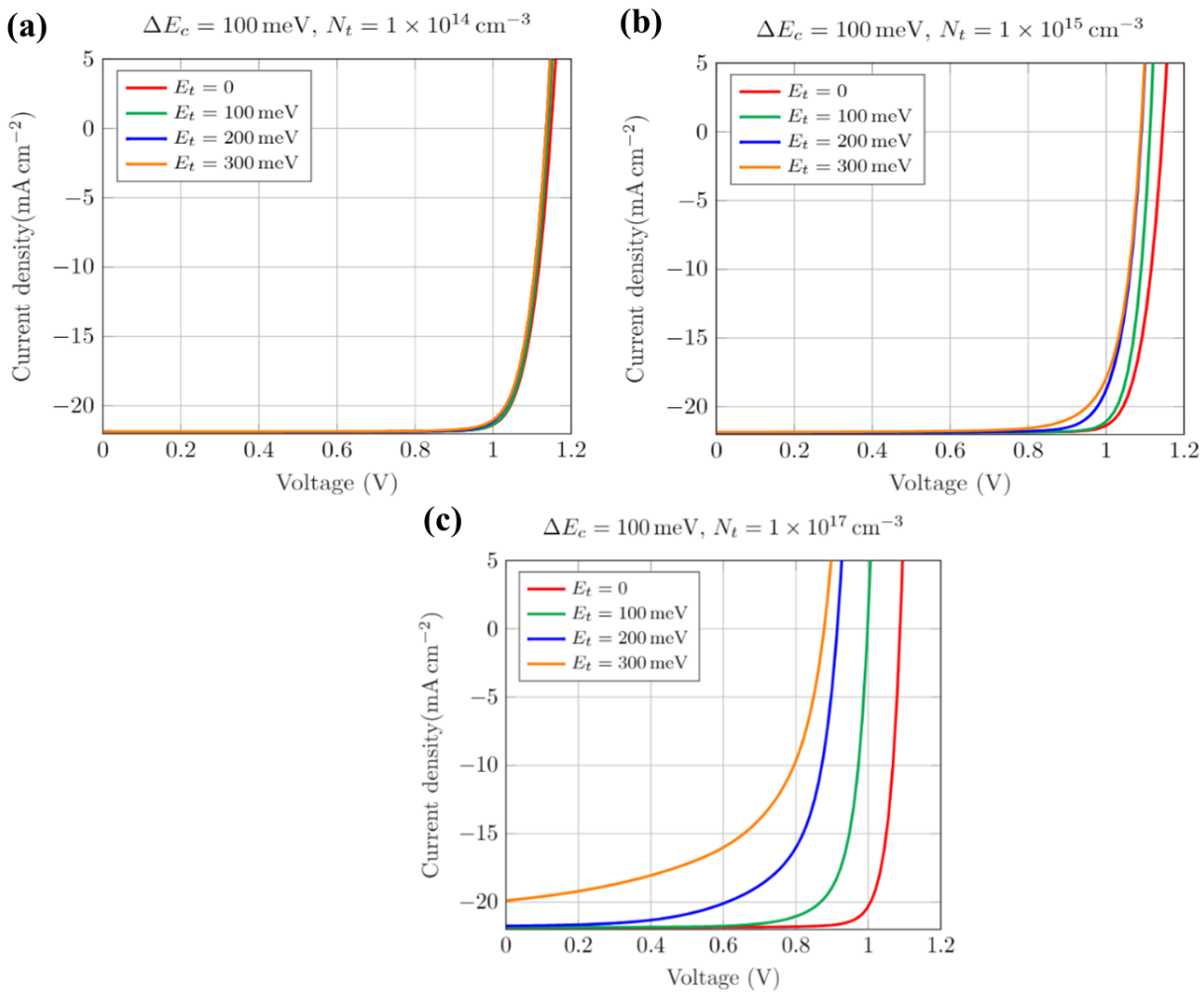

Figure S21. Calculated J-V characteristics for various trap energies (below the perovskite conduction band edge) at the grain boundaries. The grain boundary conduction band energy is considered to be 100 meV below the conduction band minima of the bulk perovskite, i.e., $\Delta E_c = 100$ meV.

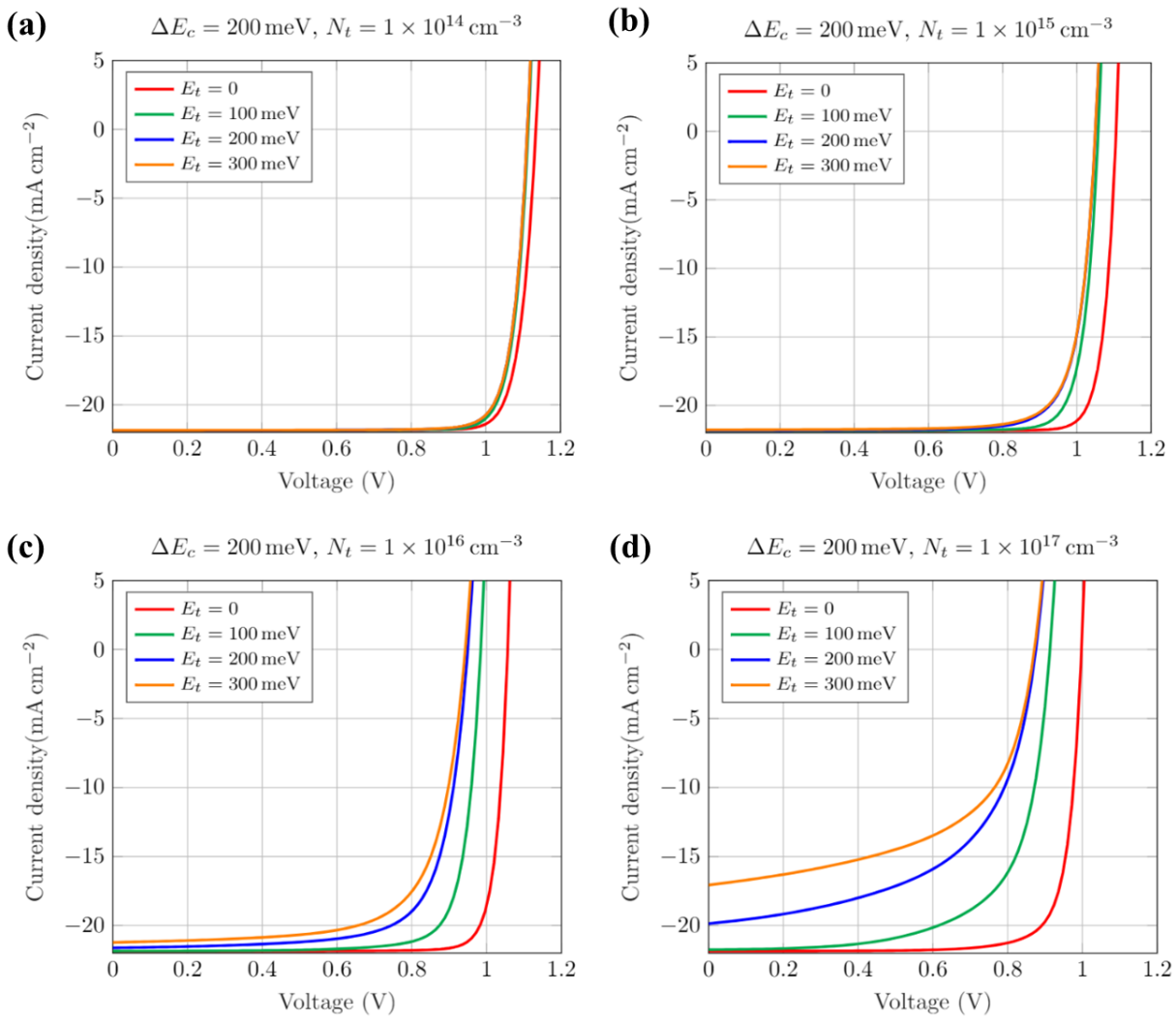

Figure S22. Calculated J-V characteristics for various trap energies (below the perovskite conduction band edge) at the grain boundaries. The grain boundary conduction band energy is considered to be 200 meV below the conduction band minima of the bulk perovskite.

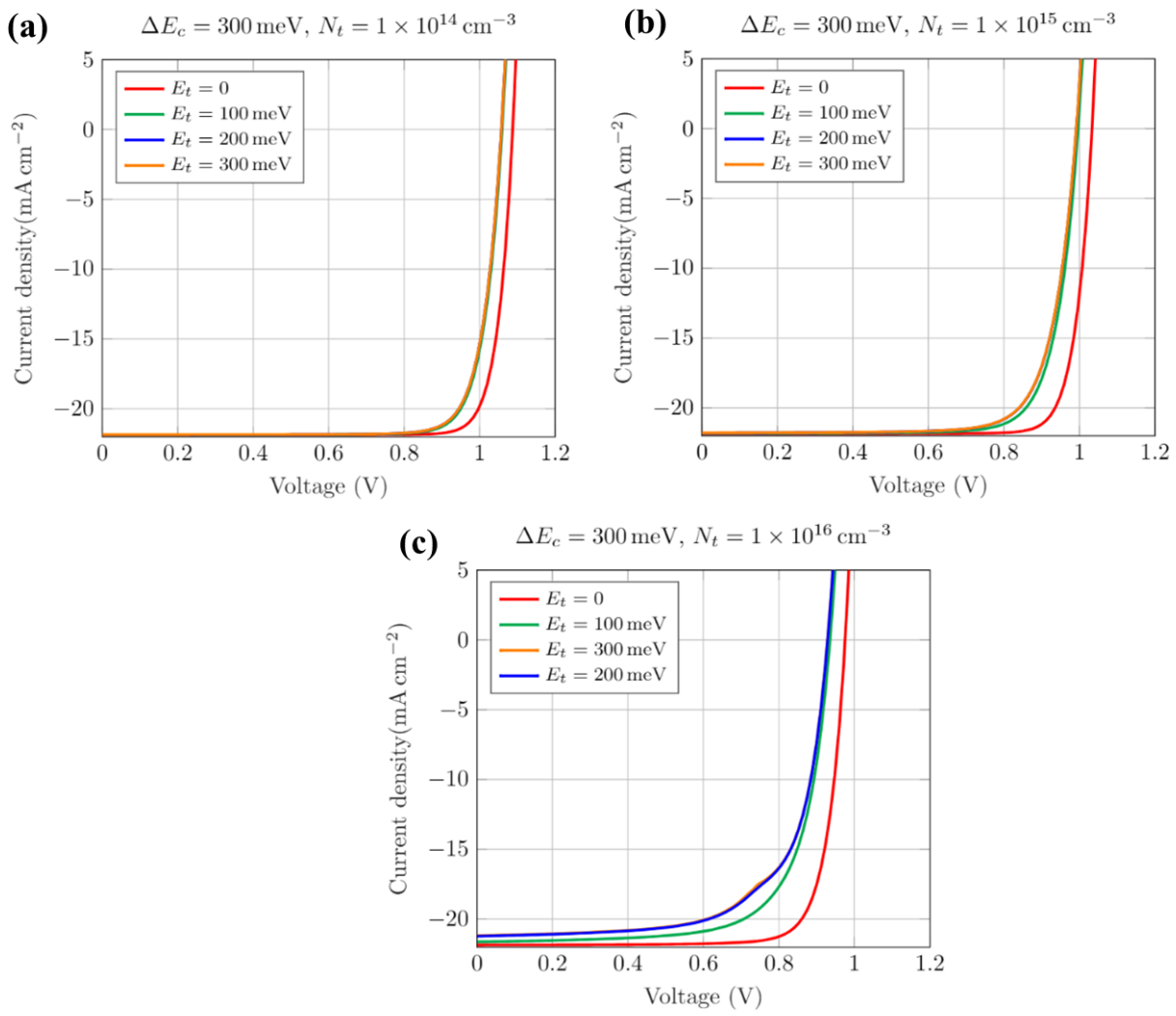

Figure S23. Calculated J-V characteristics for various trap energies, with reference to the perovskite conduction band edge, at the grain boundaries. The grain boundary conduction band energy is assumed to be 300 meV below the conduction band minima of the bulk perovskite.

References

(1) M. Auf Der Maur, G. Penazzi, G. Romano, F. Sacconi, A. Pecchia and A. Di Carlo, The Multiscale Paradigm in Electronic Device Simulation. *IEEE Trans. Electron Devices*, **2011,** 58(5). DOI:10.1109/TED.2011.2114666.

(2) A. Gagliardi, M. Auf Der Maur, D. Gentilini, F. Di Fonzo, A. Abrusci, H. J. Snaith, G. Divitini, C. Ducati and A. Di Carlo. The Real TiO_2/HTM Interface of Solid-State Dye Solar Cells: Role of Trapped States from a Multiscale Modelling Perspective. *Nanoscale*, **2015,** 7, 1136-1144, DOI: 10.1039/C4NR05208K

(3) A. Singh and A. Gagliardi, Efficiency of All-Perovskite Two-Terminal Tandem Solar Cells. *Sol. Energy*, **2019,** 187, 39–46. DOI: 10.1016/j.solener.2019.05.006.

(4) A. Gagliardi and A. Abate, Mesoporous Electron-Selective Contacts Enhance the Tolerance to Interfacial Ion Accumulation in Perovskite Solar Cells. *ACS Energy Lett.,* **2018,** 3, 1, 163–169 DOI:10.1021/acsenergylett.7b01101.

(5) A. H. Fallahpour, A. Gagliardi, D. Gentilini, A. Zampetti, F. Santoni, M. Auf der Maur and A. Di Carlo, Optoelectronic Simulation and Thickness Optimization of Energetically Disordered Organic Solar Cells, *J. Comput. Electron.,* **2014,** 13(4), pp 933–942. DOI:10.1007/s10825-014-0611-y.

(6) A. H. Fallahpour, D. Gentilini, A. Gagliardi, M. A. Der Maur, P. Lugli and A. Di Carlo, Systematic Study of the PCE and Device Operation of Organic Tandem Solar Cells. *IEEE J. Photovoltaics*, **2016,** 6(1), pp 202-210. DOI:10.1109/JPHOTOV.2015.2486382.

(7) A. Singh, E. Radicchi, S. Fantacci, F. De Angelis and A. Gagliardi, Interface Electrostatics of Solid-State Dye-Sensitized Solar Cells: A Joint Drift-Diffusion and Density Functional Theory Study. *J. Phys. Chem. C*, **2019**, 123, 24, 14955–14963, DOI: 10.1021/acs.jpcc.9b03658.

(8) D. Gentilini, A. Gagliardi, A. A. Franco, F. Sauvage and A. di Carlo, A Drift-Diffusion Study on Charge Unbalancing Effects in Dye-Sensitized Solar Cells. *J. Electrochem. Soc.,* **2015**, 16(10), DOI:10.1149/2.0061510jes.

(9) R. Tagliaferro, D. Gentilini, S. Mastroianni, A. Zampetti, A. Gagliardi, T. M. Brown, A. Reale and A. Di Carlo, Integrated Tandem Dye Solar Cells, *RSC Adv.,* **2013**,3, 20273-20280, DOI:10.1039/c3ra43380c.

(10) D. Rossi, F. Santoni, M. Auf Der Maur and A. Di Carlo, A Multiparticle Drift-Diffusion Model and its Application to Organic and Inorganic Electronic Device Simulation. *IEEE Trans. Electron Devices*, **2019**, 66(6), pp 2715-2722. DOI:10.1109/TED.2019.2912521.

(11) A. Di Vito, A. Pecchia, A. Di Carlo and M. Auf Der Maur, Impact of Compositional Nonuniformity in (In,Ga)N-Based Light-emitting Diodes. *Phys. Rev. Appl.,* **2019**, 12, 014055. DOI:10.1103/PhysRevApplied.12.014055.

(12) C. Zhang, W. Luan, and Y. Yin. High Efficient Planar-Heterojunction Perovskite Solar Cell based on Two-Step Deposition Process. *Energy Procedia*, **2017,**105:793–798. DOI: 10.1016/j.egypro.2017.03.391.

(13) C. Wehrenfennig, G. E. Eperon, M. B. Johnston, H. J. Snaith, and L. M. Herz. High Charge Carrier Mobilities and Lifetimes in Organolead Trihalide Perovskites. *Adv. Mater*., **2014**. 26(10):1584–1589. DOI: 10.1002/adma.201305172.

(14) F. Brivio, K. T. Butler, A. Walsh, and M. Van Schilfgaarde. Relativistic Quasi-Particle Self-Consistent Electronic Structure of Hybrid Halide Perovskite Photovoltaic Absorbers. *Phys. Rev. B ,* 2**014,** 89(15):155204. DOI: 10.1103/PhysRevB.89.155204.

(15) P. Tiwana, P. Docampo, M. B. Johnston, H. J. Snaith, and L. M. Herz. Electron mobility and Injection Dynamics in Mesoporous ZnO, SnO_2, and TiO_2 Films used in Dye-Sensitized Solar Cells. *ACS Nano*, **2011**, 5(6):5158–5166. DOI: 10.1021/nn201243y

(16) T. Leijtens, J. Lim, J. Teuscher, T. Park, and H. J. Snaith. Charge Density Dependent Mobility of Organic Hole-Transporters and Mesoporous TiO_2 Determined by Transient Mobility Spectroscopy: Implications to Dye-Sensitized and Organic Solar Cells. *Adv. Mat.,* **2013**, 25(23):3227–3233. DOI: 10.1002/adma.201300947.

(17) Z. Li, J. Chen, H. Li, Q. Zhang, Z. Chen, X. Zheng, et al. A Facilely Synthesized 'spiro' Hole-Transporting Material based on spiro[3,3]heptane-2,6-dispirofluorene for Efficient Planar Perovskite Solar Cells. *RSC Adv.,* **2017**, 7(66):41903–41908. DOI: 10.1039/C7RA06643K.

(18) A. J. Moul´e, H. J. Snaith, M. Kaiser, H. Klesper, D. M. Huang, et al. Optical Description of Solid-State Dye-Sensitized Solar Cells. I. Measurement of Layer Optical Properties. *J. Appl. Phys.,* **2009,** 106(7):073111. DOI: 10.1063/1.3204982.

(19) A. Wypych, I. Bobowska, M. Tracz, A. Opasinska, S. Kadlubowski, et al. Dielectric Properties and Characterisation of Titanium Dioxide Obtained by Different Chemistry Methods. *J. Nanomater.,* **2014,** 124814. DOI: 10.1155/2014/124814

(20) T. Kirchartz, J. A. Marquez, M. Stolterfoht, and T. Unold. Photoluminescence-based Characterization of Halide Perovskites for Photovoltaics. *Adv. Energy Mater.,***2020**, 10(26):1904134, 2020. DOI: 10.1002/aenm.201904134.

(21) N.-G. Park. Perovskite solar cells: An Emerging Photovoltaic Technology. *Mater. Today,* **2015**, 18(2):65–72. DOI: 10.1016/j.mattod.2014.07.007.

(22) L. Canil, T. Cramer, B. Fraboni, et al. Tuning Halide Perovskite Energy Levels. *Energy Env. Sci.,* **2021**,14, 1429-1438. DOI: 10.1039/D0EE02216K.

(23) Singh, A. Electronic-Ionic Transport in Organic-Inorganic Hybrid Perovskite Solar Cells: A Combined Theoretical and Experimental Study, P*hD Dissertation*, **2021**